Eindhoven University of Technology

BACHELOR

Dip & die-coating of chemically patterned surfaces

van Cuijk, A.W.

Award date:
2015

Technische Universiteit
Eindhoven
University of Technology

Department of Applied Physics
Mesoscopic Transport Phenomena

Dip & die-coating of chemically patterned surfaces

Bachelor Thesis

A.W. van Cuijk

Supervisors:
Dr. B. J. Brasjen
Prof. Dr. A.A. Darhuber

Final version

Eindhoven, August 2015

Abstract

The selective deposition of thin liquid films on chemically heterogeneous surfaces by means of dip and die-coating is studied. Both coating processes are methods for creating large arrays of liquid micro-structures for applications ranging from biotechnology to organic electronics. The maximum film thickness of the entrained structures is affected by the size, geometry, and angular orientation of the patterns, as well as the coating speed. The experimental results for long, thin lines agree excellently with the literature, and the effect for line widths around the capillary length is studied. Moreover, the behavior of the more exotic shapes triangles and squares are studied, whose dynamical coating process fundamentally differ from the steady-state process of narrow lines or homogeneous surfaces. Finally, the influence of the die-gap is examined, and a force balance is calculated for samples during the die-coating process.

Acknowledgements

I would like to extend my gratitute to my supervisors Berend Brasjen for being my guide in the wonderful world of coating mechanisms, and Anton Darhuber for helping me in the final stages of my project. This thesis could not have been possible without your expertise and patience.

A big thank you to my good friends from Kinjin, especially Sjaak for being right next to me all the way on the road to become a physicist, and Ruben for his help.

Completing my education would not have been possible without the help of my parents. Thank you for everything you have done.

Finally, thanks to all who supported me in any respect finishing this project.

Contents

Bibliography

Appendix

A Calculation of centroid position

List of Figures

Chapter 1

Introduction

Selective depositing thin liquid films on substrates is required in a multitude of industrial applications, ranging from biotechnology to organic electronics. A well confined and highly uniform film, as well as large coating speeds are characteristics which make a particular coating mechanism feasible for industrial use. A simple means of doing this is immersing a substrate in a liquid bath of coating material, and subsequently withdrawing it at a constant velocity. This process is called dip-coating. Figure 1.1 shows a schematic for the dip-coating process. The radius of curvature of the meniscus is denoted by R, and V is the speed at which the substrate is withdrawn from the liquid. $l_C = \sqrt{\gamma/\rho g}$ is the capillary length, a material property of the liquid, with γ and ρ the surface tension and density of the liquid, respectively. Typical values of the capillary length are 1 – 3 mm.

Dip-coating has been investigated for over seven decades, primarily focussing on chemically homogeneous substrates [5, 7]. With modern-day technology such as micro-contact printing or photo-lithography, it is possible to create substrates with wetting properties with a sub-micron resolution. Using these techniques it is possible to create a hydrophobic substrate, while certain parts in any required shape are hydrophilic. The coating of these chemically patterned surfaces has only recently been studied for low coating speeds by Darhuber and Davis [3]. The aforementioned prerequisite of a highly uniform film without defects like blisters, holes, cracks, or local material accumulation is a considerable challenge, especially at higher coating speeds.

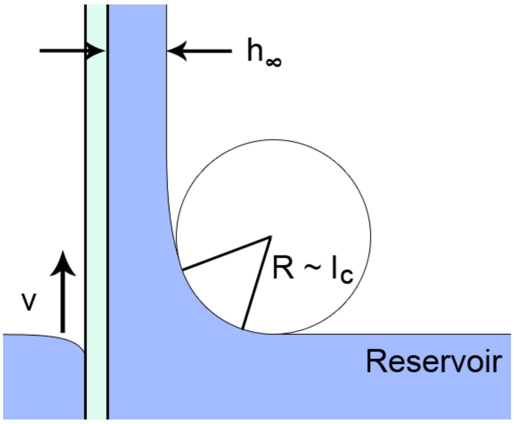

Figure 1.1: Schematic for dip-coating. A substrate is pulled out of a reservoir with constant speed V. The maximum entrained film thickness h_∞ is determined by the relevant length scale, which is the capillary length l_C.

The entrained film thickness, oriented parallel to the withdrawal direction h_∞ has been derived by Landau and Levich [7] and Deryaguin [5] for the dip-coating process of a infinitely wide, perfectly wetting substrate:

$$h_\infty = 0.946 \cdot l_C \cdot Ca^{2/3}, \tag{1.1}$$

with $Ca = \mu V/\gamma \ll 1$ the capillary number, and μ the viscosity of the liquid. The derivation assumes that the film thickness is much smaller than the length scale of the overall flow field. In this regime, the gravitational drainage is negligible, and the capillary and viscous forces balance each other out. The result is a static meniscus emanating in a flat film profile with film thickness h_∞. An extended analysis for larger values of Ca is done by White and Tallmadge [15], and a second order correction to equation equation 1.1 is derived by Wilson [16]:

$$h_\infty = l_C \cdot \left(0.946 \cdot Ca^{2/3} - 0.107 \cdot Ca\right). \tag{1.2}$$

Now consider the case of a substrate with a hydrophilic / hydrophobic patterning, for example a long and thin rivulet with a line width w much smaller than the radius of curvature of the meniscus. The associated capillary pressure will dominate the flow, and the relevant length scale will be the rivulet thickness. A rivulet is considered “long” if its length $L \geq 10w$. For such a narrow hydrophilic line, the maximum entrained film thickness has been derived by Darhuber et al. [3]:

$$h_\infty = 0.356 \cdot w \cdot Ca^{1/3}, \tag{1.3}$$

in which the proportionality constant is computed numerically by Davis [4] using an asymptotic matching technique.

Another widely used coating technique is to slide the substrate very close to a nearly parallel static die a distance h_0 away, while keeping a small provision of coating material in between. A schematic for this process known as die-coating is depicted in figure 1.2. For the liquid bridge between the two solids to remain stable, h_0, also called the die-gap, has to be smaller than the capillary length. The relevant length scale determining the meniscus shape therefore changes from l_C to h_0. Substituting this in equation 1.1 yields a relation between the film thickness and the capillary number:

$$h_\infty \propto h_0 \cdot Ca^{2/3}. \tag{1.4}$$

With its more complex structure, the die-coating problem naturally requires a more strenuous derivation, which is given by Ruschak [12]. The relatively simple analytical theoretical description of dip and die-coating is the reason these two techniques are chosen to elucidate the influence of various chemical surface patterns on the liquid entraining process.

It is clear from comparing equations 1.1 and 1.3, that the transition of the relevant length scale results in a drop in the exponent of the capillary number from 2/3 to 1/3. This behavior has been confirmed experimentally for small values of Ca [3, 11, 15]. In order to test our equipment and methods, we will start by reproducing the results of dip-coating narrow hydrophilic lines. Hereafter, we will test the limits of validity of equations 1.1 and 1.3 by focussing on the transition regime where the line width $w \approx l_C$. We also consider the film thickness of two thin lines parallel to each other with varying distance between them. Subsequently, we will study the case of square and triangular patterns of different size and angle as an example of liquid entrainment on compact patterns. No steady state analysis is applicable here and capillary break-up effects influence the process [1]. Finally, for the die-coater, experiments are done with squares and triangles of different sizes, as well as with varying the die-gap.

Figure 1.2: Schematic for die-coating. A substrate is slid underneath a die with constant speed V. The entrained film thickness h_∞ is determined by the relevant length scale, which is the die gap h_0.

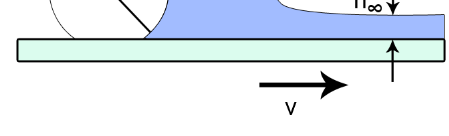

Chapter 2

Theory

2.1 Analysis of vertical forces in the die-coater

An essential matter of a well-functioning die-coater is that the substrate is not lifted up before or during the coating process. This might happen if the capillary forces produced by the bulk of the coating liquid F_{cap} are larger than the gravity force of the substrate $F_{g,sub}$, the gravity force of the liquid mass $F_{g,liq}$, and the normal component of the viscous force $F_{vis,z}$ combined:

$$F_{cap} \overset{?}{>} F_{g,sub} + F_{g,liq} + F_{vis,z}. \tag{2.1}$$

In this section it is discussed whether this might happen for a typical die-coating experiment. Figure 2.1 depicts a schematic of the die-coater, and figure 2.2 shows the approximate volume of the coater liquid. A photo of the set-up is shown in figure 3.3(c,d). θ_1 and θ_2 are the contact angles of the liquid on the substrate and the die, respectively, and φ is the inclination angle of the die. h_0 is the distance between the die and substrate at the tip of the die, and h the distance between the die and substrate at the left meniscus. h_0 shall be referred to as the die-gap, while h shall be referred to as the tail-gap. $h_1 = h - h_0$ is the difference between these two. R is the radius of curvature of the left meniscus, and l and b are the length and width of the liquid bulk. Finally, Vol is the volume of the coating liquid, and V the speed at which the substrate is moved underneath the die. The values and ranges for these variables, as well as the material properties of the used coating liquid tetraethylene glycol (TEG), are given in table 2.1.

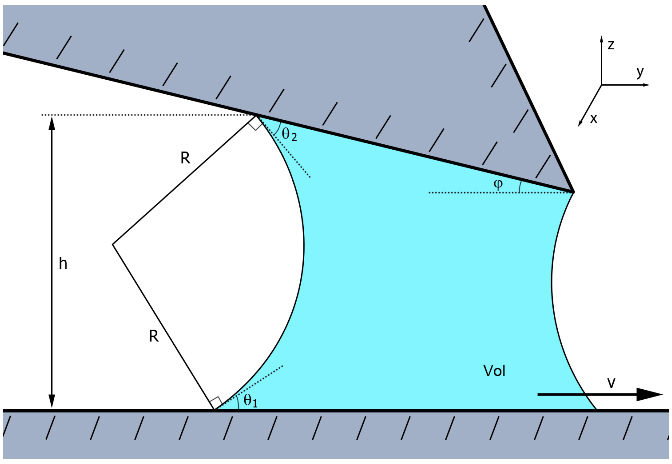

Figure 2.1: Relevant control variables for the die-coating process.

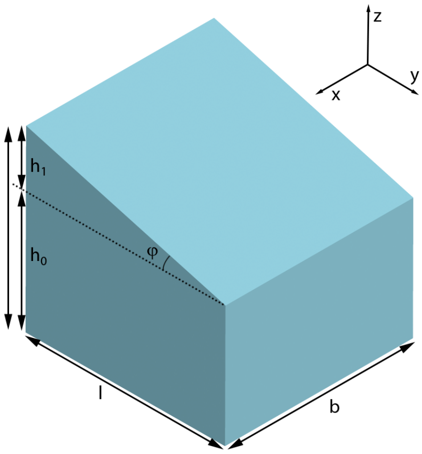

Figure 2.2: Approximate volume of the coater liquid.

Table 2.1: Typical values used in the experiments. The last four quantities come from CRC Handbook of Chemistry and Physics, 2009. Due to the hygroscopic nature, the viscosity depends on the amount of absorbed water.

θ_1 (°)	0 – 60
θ_2 (°)	45
φ (°)	∼2
h_0 (**µm**)	83 – 200
h_1 (**µm**)	∼700
h (**µm**)	800 – 1000
l (**mm**)	∼20
b (**mm**)	50
V (**µm/s**)	2.0 – 2000
μ (**mPa·s**)	58.3
γ (**mN/m**)	44.0
ρ (**kg/m^3**)	1126
l_C (**mm**)	2.00

In the stationary situation, there are no viscous forces in the system. While the substrate is moving, a Poiseuille-Couette flow arises, producing a more complex force acting from the liquid on the substrate. In order to find out whether any of these forces are much larger than the others, an analysis of the dimensionless numbers governing the flow system is used. The relative effect of viscous forces versus surface tension forces is represented by the capillary number:

$$\mathrm{Ca} = \frac{\text{viscous forces}}{\text{surface tension}} = \frac{\mu V}{\gamma}. \tag{2.2}$$

For the coating velocities given in table 2.1, the capillary number ranges from $10^{-6} < \mathrm{Ca} < 10^{-3}$. This means that even at the fastest die-coating experiments, the viscous forces are much smaller than the surface tension forces, and the former may be neglected. Equation 2.1 becomes:

$$F_{cap} \overset{?}{>} F_{g,sub} + F_{g,liq}. \tag{2.3}$$

The Bond number gives the relative effect of the surface tension forces compared to the body forces. It will decide whether either the capillary force or the gravity forces may be neglected:

$$\mathrm{Bo} = \frac{\text{surface tension}}{\text{body forces}} = \frac{\rho g h^2}{\gamma}. \tag{2.4}$$

Given the typical values of the tail-gap h in table 2.1, the Bond number ranges from $\mathrm{Bo} \sim 0.2$, meaning that the gravity forces and capillary forces are around the same order of magnitude. None of the terms in equation 2.3 may be neglected.

2.1.1 The viscous force

Assume that the shape of the meniscus at the left side of the liquid is circular. This is a reasonable conjecture for the a tail-gap the size of about half the capillary length. For this perfect circular form, it is possible to obtain a simple relationship between for the radius of curvature as a function of some of the control variables:

$$R = R\left(h, \theta_1, \theta_2, \varphi\right). \tag{2.5}$$

In order to find this relation, first draw two auxiliary lines passing through the contact point on the surface, perpendicular to that surface. Define A as the contact point on the substrate, B as the contact point on the die, and A' and B' as the intersection of the auxiliary lines and the

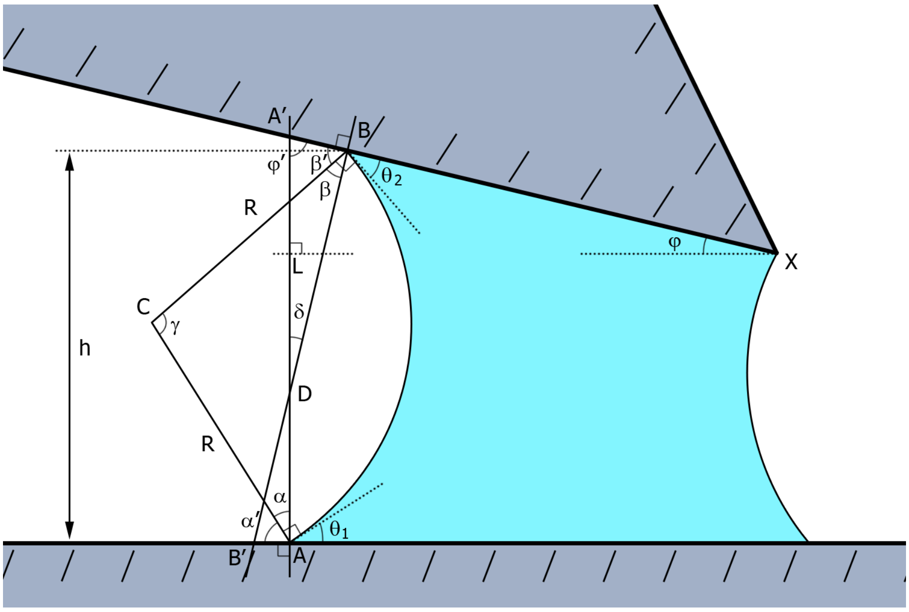

Figure 2.3: Diagram for obtaining γ.

opposite surface. Define D as the intersection of these two lines, and C to be the center of the arc of the meniscus. X is the tip of the die, and L is the intersection of the horizontal through X and the line AA'. The angles α, α', β, β', γ, δ, and φ' are as given in figure 2.3.
First the angle γ has to be calculated. In order to do this, α, β, and δ have to be expressed in terms of the known variables. Consider the triangle XLA'. As per the triangle theorem, the sum of the three angles must be π. It follows that:

$$\pi = \varphi + \frac{\pi}{2} + \varphi'$$
$$\varphi' = \frac{\pi}{2} - \varphi.$$

Now consider triangle DBA'. It follows from the same theorem that:

$$\pi = \delta + \frac{\pi}{2} + \left(\frac{\pi}{2} - \varphi\right)$$
$$\delta = \varphi.$$

The sum of the angles $\theta_1 + \frac{\pi}{2} + \alpha' = \pi$, for it is a straight angle:

$$\alpha' = \frac{\pi}{2} - \theta_1. \tag{2.6}$$

Furthermore, the sum of the angles $\alpha + \alpha' = \frac{\pi}{2}$, for it is a right angle:

$$\alpha = \frac{\pi}{2} - \left(\frac{\pi}{2} - \theta_1\right) \tag{2.7}$$
$$\alpha = \theta_1.$$

Analogous to equations 2.6 and 2.7, it can be derived that $\beta = \theta_2$. Now consider $ACBD$. The total sum of the interior angles of this quadrilateral is 2π. Since α, β, and δ are known, γ can be obtained:

$$2\pi = (\alpha) + (\beta) + (\gamma) + (\pi + \delta)$$
$$2\pi = \theta_1 + \theta_2 + \gamma + \pi + \varphi$$
$$\gamma = \pi - \varphi - \theta_1 - \theta_2. \tag{2.8}$$

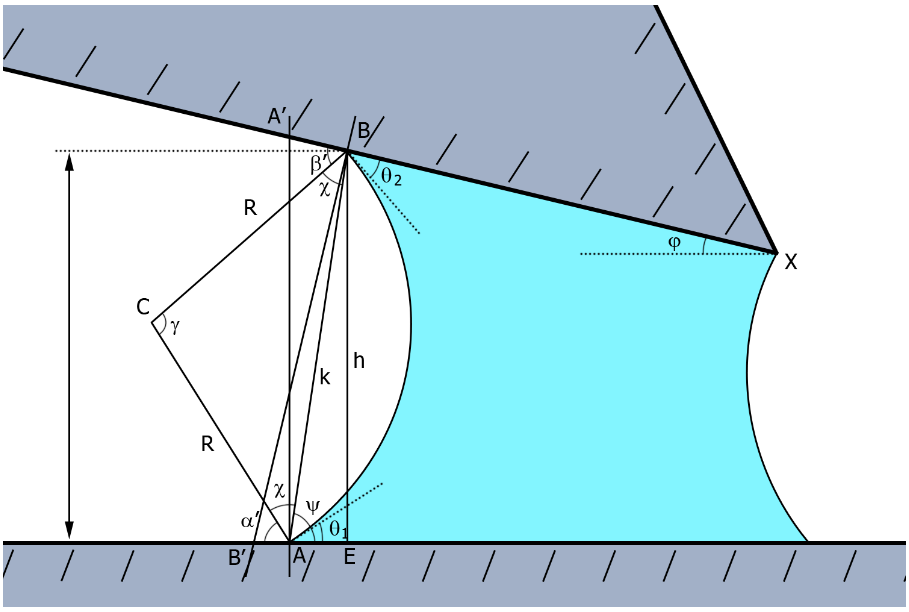

Figure 2.4: Diagram for obtaining R.

Define point E as the vertical on the substrate passing through B, which has a known length h. k is the chord AB. Since $AC = BC = R$, ABC is an isosceles triangle. The angles in this triangle are χ. ψ will be the angle between k and the substrate. Figure 2.4 shows this schematically. Consider isosceles triangle CAB. Conform the triangle theorem, it follows that:

$$\begin{aligned}\pi &= \gamma + \chi + \chi \\ \chi &= \frac{\pi - \gamma}{2}.\end{aligned}$$

The sum of the angles along point A is π, because it is a straight angle:

$$\begin{aligned}\pi &= \alpha' + \chi + \psi \\ \pi &= \left(\frac{\pi}{2} - \theta_1\right) + \left(\frac{\pi - \gamma}{2}\right) + (\psi) \\ \pi &= \frac{\pi}{2} - \theta_1 + \frac{\pi - (\pi - \varphi - \theta_1 - \theta_2)}{2} + \psi \\ \psi &= \frac{\pi}{2} + \frac{\theta_1 - (\theta_2 + \varphi)}{2} \qquad (2.9)\end{aligned}$$

Now that the angle ψ is known, the length of the chord k can be expressed in terms h. Alternatively, k can be expressed in terms of R. After finding both expressions, k can be eliminated, thus equating h to R. First, to relate k to h, consider triangle ABE:

$$\begin{aligned}\frac{h}{k} &= \sin(\psi) \\ \frac{h}{k} &= \sin\left(\frac{\pi}{2} + \frac{\theta_1 - (\theta_2 + \varphi)}{2}\right) \\ h &= k \cdot \cos\left(\frac{\theta_1}{2} - \frac{\theta_2 + \varphi}{2}\right) \qquad (2.10)\end{aligned}$$

Similarly, to relate k to R, consider triangle ABC:

$$\begin{aligned}
\frac{\left(\dfrac{k}{2}\right)}{R} &= \cos(\chi) \\
\frac{k}{2R} &= \cos\left(\frac{\pi - (\pi - \varphi - \theta_1 - \theta_2)}{2}\right) \\
k &= 2R \cdot \cos\left(\frac{\theta_1}{2} + \frac{\theta_2 + \varphi}{2}\right) \qquad (2.11)
\end{aligned}$$

Combining equations 2.10 and 2.11, the chord k can be eliminated, and after applying a trigonometric identity, relation 2.5 can be determined:

$$\begin{aligned}
h &= 2R \cdot \cos\left(\frac{\theta_1}{2} + \frac{\theta_2 + \varphi}{2}\right) \cdot \cos\left(\frac{\theta_1}{2} - \frac{\theta_2 + \varphi}{2}\right) \\
h &= R \left\{\cos(\theta_1) + \cos(\theta_2 + \varphi)\right\} \\
\frac{1}{R} &= \frac{1}{h} \left\{\cos(\theta_1) + \cos(\theta_2 + \varphi)\right\} \qquad (2.12)
\end{aligned}$$

The capillary force can be found by calculating the pressure difference inside and outside the liquid, and multiplying it by the total contact area of the liquid with the substrate. The pressure inside the liquid is defined by the Young-Laplace equation [6]:

$$\Delta p = \gamma \left(\frac{1}{R_1} + \frac{1}{R_2}\right), \qquad (2.13)$$

with Δp the pressure gradient across the fluid interface, γ the surface tension of the liquid, and R_1 and R_2 the principal radii of curvature in the yz-plane (parallel to the substrate) and the xy-plane (perpendicular to the substrate), respectively. This equation can be simplified, because $h \ll l, b$, making the radius of curvature parallel to the plate is much larger than the radius of curvature perpendicular to it: $R_1 \gg R_2$, or $R_1^{-1} \ll R_2^{-1}$. Hence, for the pressure gradient:

$$\begin{aligned}
\Delta p &= \gamma \left(\cancel{\frac{1}{R_1}} + \frac{1}{R_2}\right) \\
\Delta p &= \frac{\gamma}{R} \\
\Delta p &= \frac{\gamma}{h} \left\{\cos(\theta_1) + \cos(\theta_2 + \varphi)\right\}. \qquad (2.14)
\end{aligned}$$

Note that the contact angle at the tip of the die is not well defined. The meniscus will shape itself so that the pressure gradient equals that of the other side. Indeed, if it did not, a pressure would arise inside the liquid, which would result in a Poiseuille flow. Since the pressure is constant all over the liquid, the capillary force F_{cap} can easily be found by multiplying the pressure by the contact area $A = lb$:

$$\begin{aligned}
F_{cap} &= \Delta p \cdot A \\
F_{cap} &= \frac{\gamma l b}{h} \left\{\cos(\theta_1) + \cos(\theta_2 + \varphi)\right\}. \qquad (2.15)
\end{aligned}$$

For the data given in table 2.1, the capillary force ranges from $F_{cap} = 58 - 92$ mN, with the situation of the lowest gap distance $h \approx 800\mu$m and complete wetting with a contact angle $\theta_1 = 0°$ accounting for the upper range.

2.1.2 The gravity forces

The weight of the liquid can be estimated by approximating the liquid as in figure 2.2. This is warranted, because $h \ll l, b$, making the error in the boundary volume in the simplified model much smaller than the bulk of the liquid. The total volume Vol is now the sum of the cuboid below the dotted line and the triangular prism above it:

$$Vol = (h_0 lb) + \left(\frac{1}{2} h_1 lb\right)$$
$$Vol = lb\left(h_0 + \frac{l}{2}\tan\varphi\right).$$

This yields for the gravity force of the liquid:

$$F_{w,liq} = mg = \rho V g = \rho g l b\left(h_0 + \frac{l}{2}\tan\varphi\right). \tag{2.16}$$

Using the data in table 2.1, the gravity force of the coating liquid is about $F_{w,liq} = 17$ mN, which is in the order of magnitude expected for a Bond number of 0.2.

The substrate is a glass plate with dimensions $Vol_{sub} = 50 \times 75 \times 1$ mm^3. Because the thickness of the chemical film on the substrate is in the order of nanometers, the weight film deposited on top of the glass is negligible compared to the total weight of the substrate. The density of the used D263 glass is given by the manufacturer, and is $\rho = 2510$ kg $\cdot$ m^{-3}. The substrate weight can now be calculated:

$$F_{w,sub} = mg = \rho Vol_{sub} g.$$

This yields $F_{w,sub} = 92$ mN. Combining the numerical values of all variables in equation 2.3:

$$F_{cap} \overset{?}{>} F_{g,sub} + F_{g,liq}$$
$$92\text{mN} \not> 92\text{mN} + 17\text{mN}.$$

It follows that for this case study the substrate will not be lifted up to the die, although small errors in the set-up may precipitate this event anyway.

2.2 Calculating the maximum height

The maximum height of a bubble can be calculated by using a white-light interferometer. As with any optical interferometer, the apparatus relies on the splitting of an optical beam in two parts. Figure 2.5 gives a schematic for an interferometer using a Mirau objective. These objectives are commonly used for magnifications ranging from 10 – 100×.

For the visualization of the microscopic structure, a setup similar to a standard optical microscope is taken, with a light source and a system of one or more lenses focussing the beam onto a beamsplitter, a detector array, and an interferometry objective. In figure 2.5(b), the path of a single light beam is shown through the Mirau objective, consisting of a microscope objective, two more beamsplitters, and a single completely reflective mirror to reflect the reference beam [13].

For any given wavelength λ, by varying the distance in between the interferometer and the substrate D, the total path difference of the two beams are varied differently, giving rise to constructive interference, destructuve interference, or anything in between. The brightest interference pattern is measured for constructive interference, and will happen when the difference in path length of the two beams $\Delta = 2d$ is a multiple of the wavelength of the light [10]:

$$\Delta = m \cdot \lambda.$$

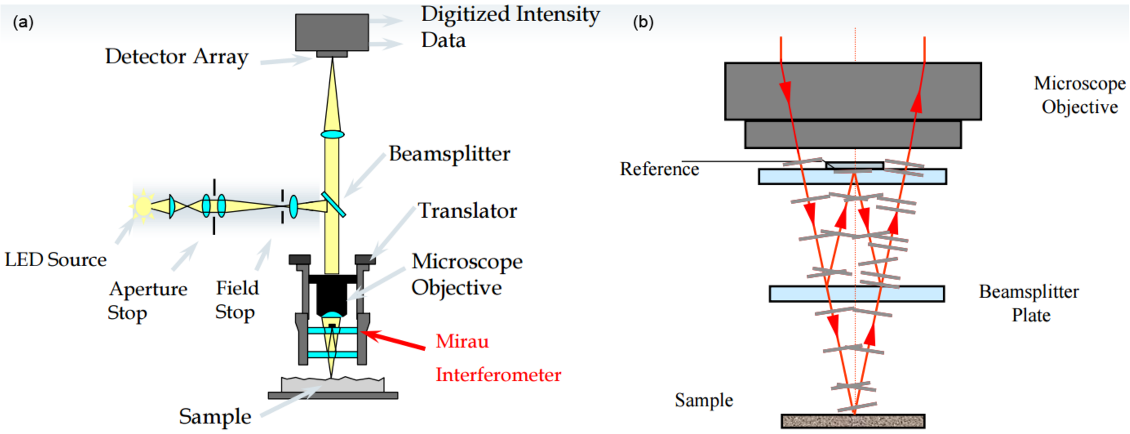

Figure 2.5: Schematic of a white-light interferometer: (a) the complete set-up, and (b) close-up of the Mirau interferometer.

with m an integer. When using white light, the problem of not knowing the mode m is circumnavigated. Since white light consists out of a wide array of wavelengths, only $m = 0$ will constitute constructive interference for the whole array, resulting in the starkest contrast in the measured interference pattern. Finding this contrast thus means that D is exactly the same for any given measurement. The maximum height for a bubble h_{max} can now be found by calculating the difference between the height at the glass plate, and the height at the top of the bubble, as shown in figure 2.6.

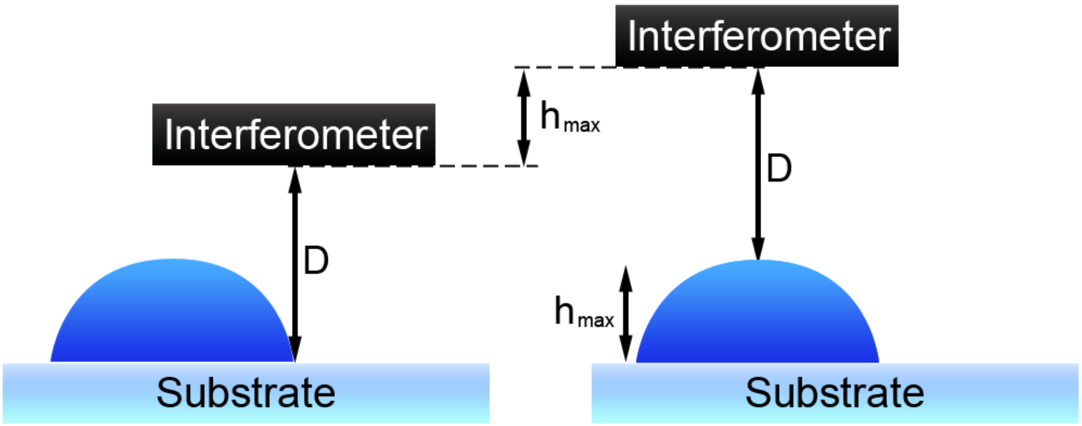

Figure 2.6: Measuring h_{max} by calculating the difference between the height of the interferometer at the top and at the bottom of the bubble.

Chapter 3

Experimental set-up

3.1 Samples

The samples are fabricated via a photo-lithographic process from 75 × 50 mm large D263 glass. The manufacturing process is depicted graphically in figure 3.1 and is completely done in a clean-room environment. To start the process off, the samples are cleaned in a 1:1:2 mixture of 98% pure sulfuric acid, 30% pure H_2O_2, and 18 MΩ distilled water. A thin layer of AR-P 3510 positive photo-resist is spin-coated onto the substrate, using HMDS as an adhesion promoter (figure 3.1(a)). To determine the difference between the future hydrophilic and hydrophobic parts of the sample, the photo-resist layer is then exposed to UV light using a mask printed on a transparency (figure 3.1(b)). The exposed parts of the layer are removed with AR 300-35 developer (figure 3.1(c)). The sample is then immersed in a solution of the hydrophobic tailed molecule 1H,1H,2H,2H-perfluorooctyltrichlorosilane (PFOTS) for 10 minutes to deposite a hydrophobic layer on the exposed areas(figure 3.1(d)). Lastly, the remaining unexposed photoresist is stripped with acetone (figure 3.1(e)) and post-cleaned with isopropanol and DI-water. The sample is now ready for coating (figure 3.1(f)).
The mono-layer of PFOTS has a thickness in the order of a few nanometers, allowing for the conjecture that the substrate as a whole is completely flat. Any excess dirt accumulated on the samples during the experiments is cleaned off using isopropanol and DI-water. After a few of these cleaning cycles, the more rigorous method for untreated glass slides is used.

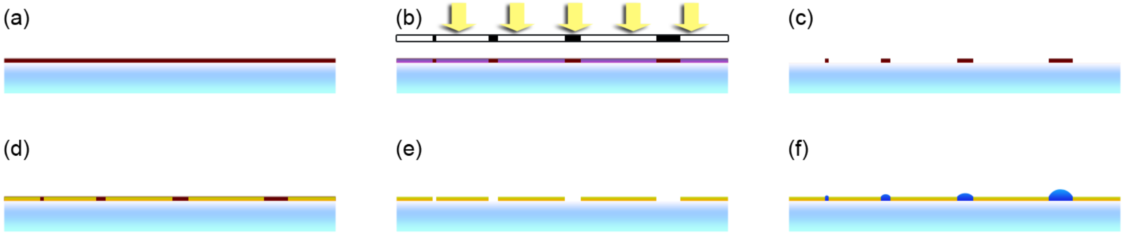

Figure 3.1: The sample manufacturing process. See text for details.

The chemical patterns used in the experiments are shown in figure 3.2. Figure 3.2(a) is a typical sample used for the measurement of various rivulet widths w, all 50 mm long and and three on one sample. In all cases, the length of the rivulets is $L \geq 10w$, so that they can be considered ‘long’. Figure 3.2(b) shows a sample used for the measurement pairs of rivulets with a varying parallel distance between them $s \lesssim l_C$, all with a length of 50 mm, and width w. Two rivulet pairs a reside on a single sample. A typical sample of squares with bases ranging from $b = 0.5 - 4.0$ mm is shown in figure 3.2(c). The squares are positioned in 5 by 4 matrix structure, increasing

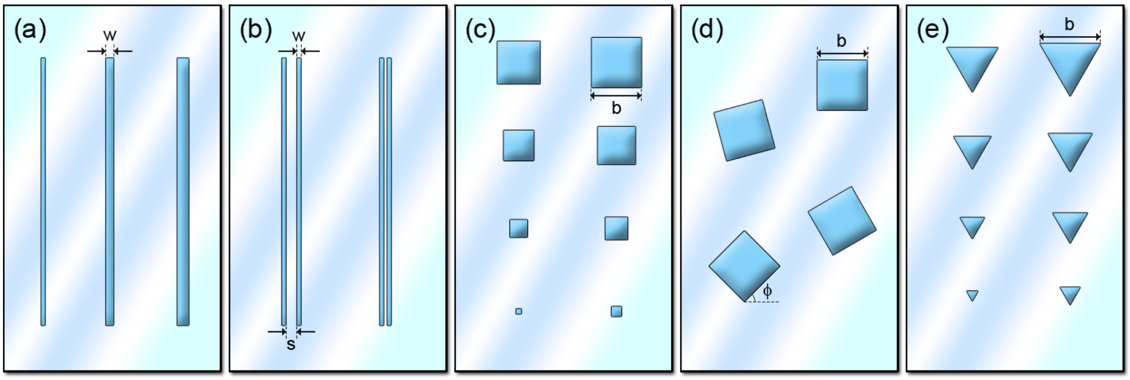

Figure 3.2: Schematic of the samples used in the experiments: (a) isolated rivulets of width w; (b) pairs of rivulets with width w and inter-rivulet distance s; (c) squares of various base lengths b; (d) squares of various inclination angles ϕ and fixed base length; (e) triangles of various base lengths.

gradually in size. The sample of figure 3.2(d) has squares with a base of $b = 4.0$ mm, but varying orientation angles $\phi = 0 - 45°$ in steps of 5°. The ten squares are segregated over the sample. Finally, figure 3.2(e) depicts triangles with bases varying between $b = 0.5 - 4.0$ mm, and have the same outline as the squares of various sizes.

3.2 Equipment

Both coating processes are done using tetraethylene glycerol (TEG) as a coating fluid. TEG is practically non-volatile, but is hygroscopic, meaning that even at very slow coating speeds virtually none of the entrained liquid evaporates, but any absorbed water vapor from the air might change the viscosity and surface tension. Its material properties are listed in table 2.1. The contact angle for TEG on the hydrophobic parts is around 60°, while the hydrophilic parts have a contact angle of 0°.

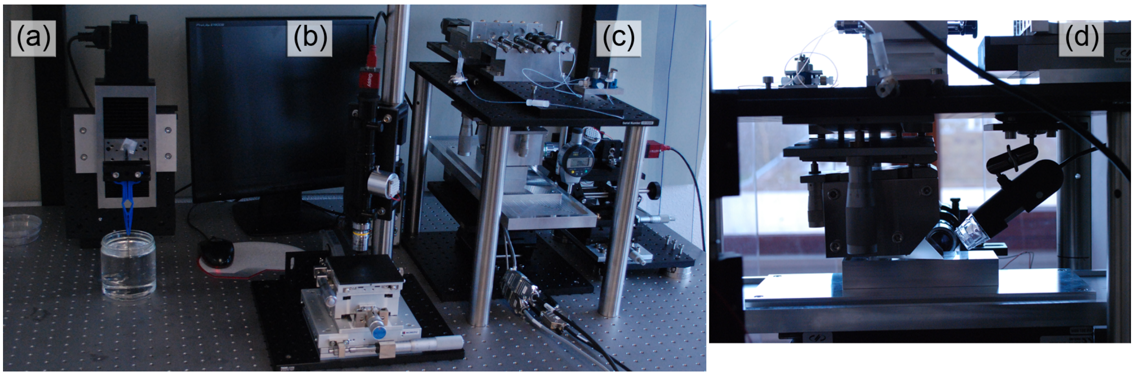

Figure 3.3: The experimental set-up: (a) the dip-coater; (b) the white-light interferometer; (c, d) the die-coater.

3.2.1 Dip-coater set-up

The dip-coater (figure 3.3(a)) consists of a computer controlled linear translation stage, powered by a DC motor with a maximum speed of 40 mm/s. A plastic forceps is used to attach the samples to the stage, allowing the gravity to align them vertically. To minimize the particle contamination, the complete setup is placed inside a laminar flowbox. The coating speed is the control parameter in this setup, and can be used to control the capillary number of the flow system.

3.2.2 Die-coater set-up

For die-coating, the substrate lies upon a metal support mounted onto a Newport XMS160 computer-controlled translation stage, which can operate at speeds ranging up to 300 mm/s. A transparent glass prism serves as the die, and is manually positioned above the substrate. This allows control over the die-gap and the two horizontal axes of rotation perpendicular and parallel to the coating direction. A finite volume of TEG is injected between the substrate and the die, where capillary forces confine it to a stable conformation.

Even though the theory in section 2.1 ensues that the sample will not be lifted up to the die, the extra force required to do so is relatively small. To ensure that no unfortunate combination of deviations in l, φ, and h_0 will make the substrate move, a few droplets of TEG are placed between the substrate and its metal support. This creates an extra capillary force on the right-hand side of equation 2.3.

During all the experiments, the die is tilted around 2° so that the die-gap is smaller than the tail-gap. The axis of control perpendicular to the coating direction is held constant such that the die-gap is the same at both sides of the sample. In this set-up, there are two important control parameters to control the flow system. The coating speed controls the capillary number, and the die-gap controls the relevant length scale of the system.

3.2.3 Interferometer set-up

After the coating process is complete, the sample is immediately put in a horizontal position given 10 − 15 minutes to let the films equilibrate. A home-built white-light interferometer is used to measure the thickness of the entrained films h_{max}. It is built using a Infinitube, a Nikon CF IC Epi Plan DI 10× interferometry objective, and a broad-spectrum light source. A Kohzu ZM10A-C3C manual z-stage is used to control the distance between the sample and the objective, and it is measured using a Mitutoyo ID-H0530 digital indicator with an accuracy of 1–2 μm. The Kohzu stage converts horizontal motion to vertical motion with a conversion factor of 0.25, thus enabling local height measurement with a resolution of 0.125 μm and an accuracy of 0.5 μm.

The measurement of the maximum film thickness h_{max} is done in a dark room. Typical interference images are depicted in figure 3.4. Figure 3.4(a) shows a typical example of a well-defined triangle. Figure 3.4(b) shows a triangle with a receded contact line in respect to the hydrophilic patterning. Typically, this problem could not be resolved by cleaning the sample, indicating that the hydrophilic / hydrophobic interface is unsatisfactory. Primarily the small triangles and squares with bases $b < 0.9$ mm had this problem, and they are not measured. Figure 3.4(c) gives a typical example of a triangle that is contaminated with dust particles. If a pattern had many dust particles, the sample was cleaned and the pattern was measured again. The error in the measurements is primarily determined by how well the patterns wet and how contaminated they are.

To speed up the data acquisition, a TI-83 Plus graphical calculator was programmed to calculate the position of the theoretical centroid of the 2D hydrophilic surface, while also accounting for the slightly slanted surface of the z-stage relative to the interferometer. A typical program used for the triangles can be found in Appendix A. h_{max} is given by the difference in the z-stage height for this centroid and the z-stage height for the starkest interference at these coordinates, as is shown in figure 2.6.

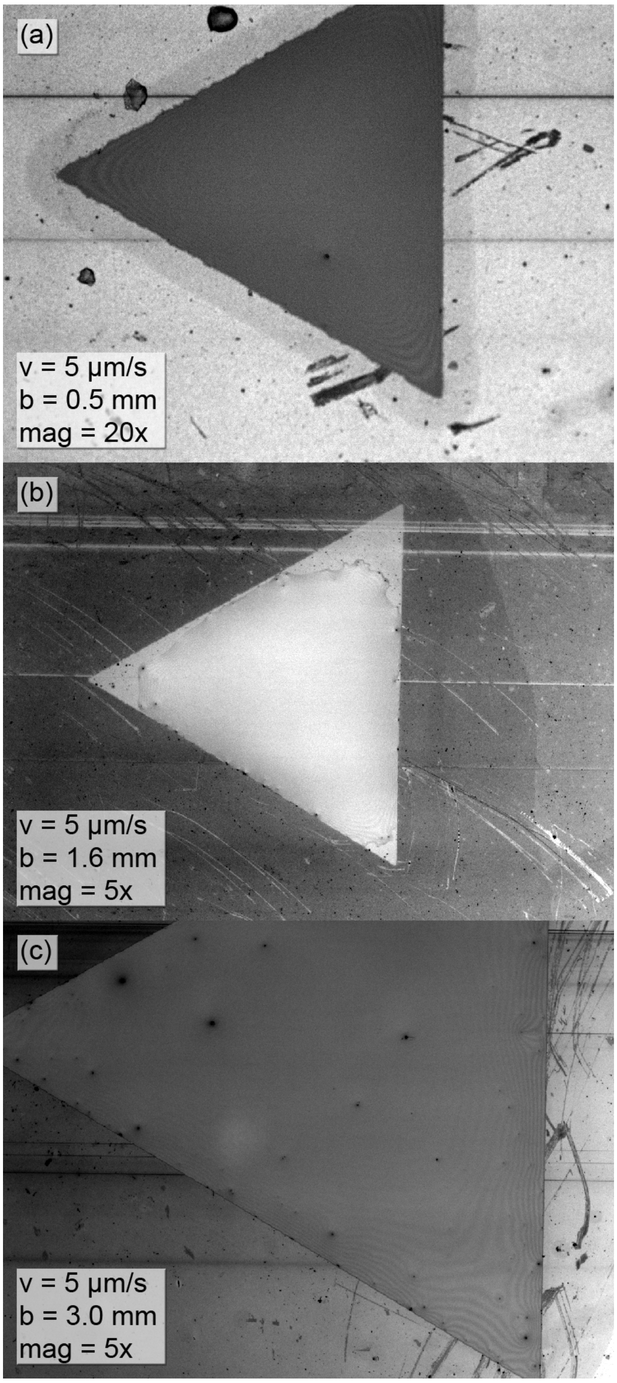

Figure 3.4: Typical contrast adjusted white-light interferometry images of dip-coated triangles with given coating speeds V*, vertice lengths* b*, and zooming magnitudes* mag*: (a) a well-defined triangle; (b) a triangle with a receded contact line; (c) a triangle with many dust particles.*

Chapter 4

Experimental results

A systematic study of the behavior of the dip-coating of hydrophilic rivulets and pairs of rivulets, as well as the dip and die-coating of hydrophilic triangles and squares was done. Dip-coating experiments were done for rivulets with varying widths w, rivulet pairs with varying parallel distance s, and triangles and squares with varying base length b. Subsequently, the effect of the inclination angle of the squares ϕ was studied. In all these experiments, the coating speed V was varied and the resulting maximum height of the droplets h_{max} was measured.
Next, the die-coating of triangels and squares with varying base length and coating speeds were examined, while keeping the die-gap constant. Finally the influence of the die-gap was studied, while maintaining a constant coating speed.
All experiments were done in the regime $10^{-6} < \mathrm{Ca} < 10^{-3}$. In this range the linear correction proposed by Wilson can be neglected. The coating fluid was TEG, of which the material properties can be found in table 2.1.

4.1 Dip-coating of rivulets

The relation between the coating speed and the entrained maximum film thickness was measured for line widths varying from 0.35 – 3.20 mm, or 0.18 l_C – 1.6 l_C.The coating speeds were varied from 10 – 100 μm/s, and the length of the lines was 50 mm. h_{max} is the average of seven measured points over the center line of the rivulet. The measured thickness was normalized with respect to the dominant length scale: w for line widths $w < l_C$, plotted on the left ordinate axis with opaque symbols, and l_C for line widths $w \geq l_C$, plotted on the right ordinate axis with open symbols. The data is plotted in figure 4.1. The dashed lines are given by equations 1.1 and 1.3.

The data for $w < l_C$ corresponds excellently with equation 1.3 and the results of [1, 3]. The two other series with $w \approx l_C$ resemble equation 1.1 more. The behavior of the dip-coating process is not defined by the theory in this region, yet the transition from the equation 1.3 to equation 1.1 is expected.
The scatter in the data might be attributed to a combination of the imperfections of the chemical patterning, the hygroscopic nature of TEG, and the contamination of the liquid bubble [1]. Imperfections in chemical patterning are probably not the cause, because remeasuring the same sample again should give the same deviation, which was not the case. Water absorbed by the TEG due to its hygroscopic nature results in a reduction in viscosity and an increment in the surface tension of the droplet. According to [2, 8], an absorbed mass of 10% of the film mass would decrease the viscosity by 20%, and increase the surface tension by 1.4 mN/m. Because of the 1/3 or 2/3 power law, the change in viscosity constitutes to the growth in droplet height by 7% or 14%, respectively. The change in viscosity is therefore negligible for the scatter in film thickness. Analogously to this reasoning, the absolute change in surface tension can not explain the scatter in data either. However, the presence of insoluble surfactants induce a surface tension that is known to increase

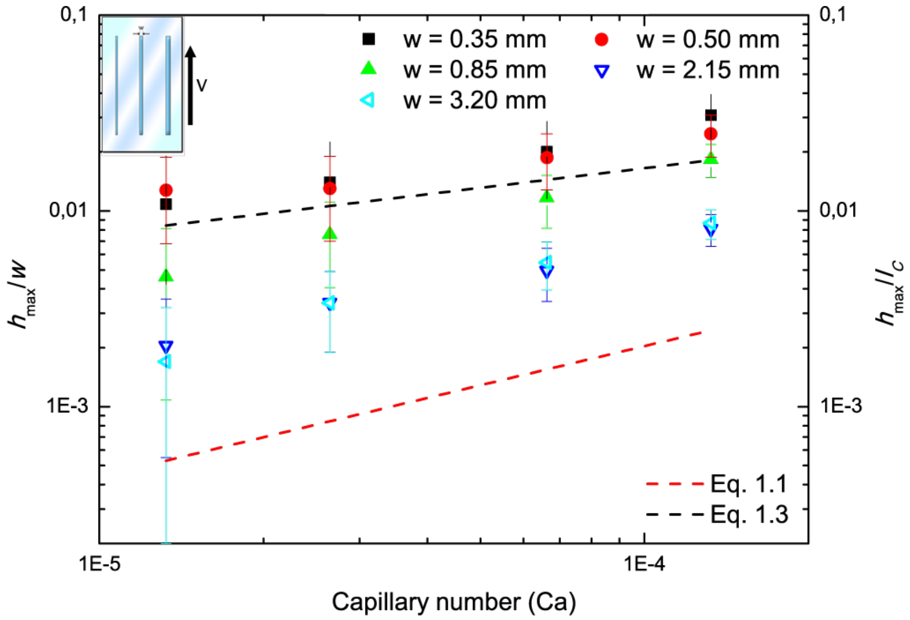

Figure 4.1: Normalized film thickness versus the capillary number; dip-coated rivulets of various widths w.

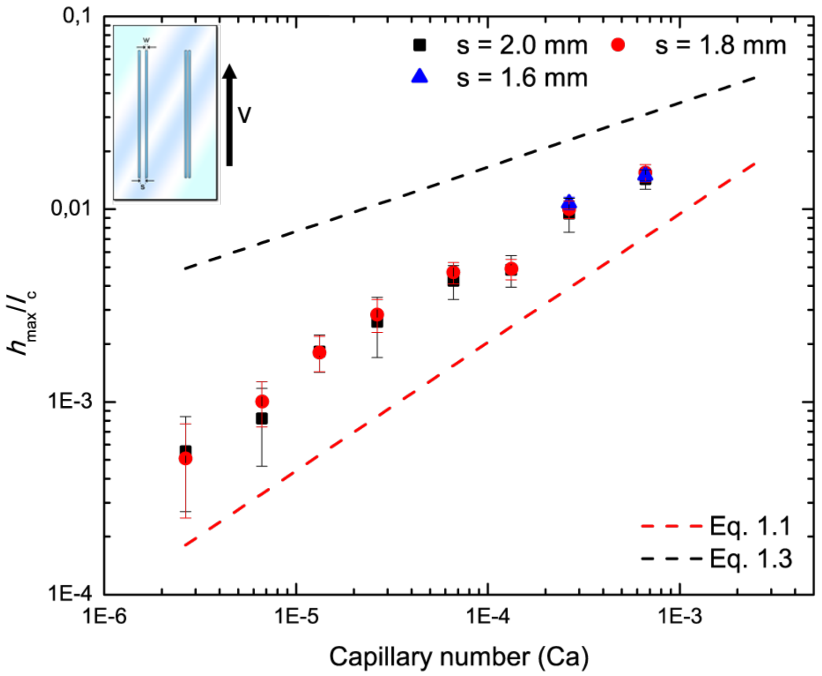

Figure 4.2: Normalized film thickness versus the capillary number; dip-coated rivulet pairs of width $w = 1.0$ mm at various parallel distances s.

film thickness by factors up to $4^{1/3}$ for narrow and $4^{2/3}$ in the case of homogeneous surfaces [9, 14]. Finally, the contamination from dust particles is expected to increase the measured film thickness.

4.2 Dip-coating of rivulet pairs

In comparison to single rivulets, the maximum height of rivulets pairs were measured. The width of the rivulets was 1.0 mm, or 0.50 l_C, their length 50 mm, and the parallel distance between the rivulets was varied from 1.6 – 2.0 mm, or 0.8 l_C – 1.0 l_C. Lower values of parallel distances resulted in a liquid bridge forming between both rivulets. The coating speeds ranged from 2 – 500 μm/s. h_{max} was measured by averaging seven measured points over the center line of the rivulets. The measured maximum height was normalized in respect to the capillary length. The data is plotted in figure 4.2. The dashed lines are given by equations 1.1 and 1.3.

Comparing the rivulet doublets to the singlets for the same capillary number, h_{max} is notably smaller for the doublets. The overall trend of the double rivulets resembles equation 1.1 more than it resembles 1.3, indicating that the rivulet pair as a whole behaves more like a single rivulet with a apparent width of $w' = 2w + s$, than than single rivulets with widths of 1.0 mm. The error in the measurements is too large draw conclusions about varying the the parallel distance. To the best knowledge of the author, no theoretical descriptions or measurements about coating multiple patterns with overlapping menisci exist to validate or compare this data to. Further research is suggested.

4.3 Dip-coating of triangles

The maximum film thickness of the entrained liquid as a function of the coating speed is measured for triangles with base lengths varying from 0.90 – 4.00 mm or 0.45 l_C – 2.0 l_C. The coating speeds range from 5 – 1000 μm/s. h_{max} was measured by calculating the position of the centroid and measuring the film thickness at that location. The measured thickness was normalized with respect to the dominant length scale: b for base lengths $b < l_C$, plotted on the left ordinate axis with opaque symbols, and l_C for base lengths $b \geq l_C$, plotted on the right ordinate axis with open symbols. The measured film thickness versus the base length is plotted in figure 4.3, and the normalized film thickness versus the capillary number is plotted in figure 4.4. The dashed lines are given by equations 1.1 and 1.3. The triangles are coating in a 'tip-down' position, as seen in the figure.

For large base lengths $b \gtrsim l_C$, the entrained film thickness saturates at a speed dependent value. Due to experimental difficulties for the triangles at $b < 0.9$ mm, no data is obtained for these low base lengths, and no conclusions can be drawn for these low base lengths. The overall behavior resembles that of the rivulets quite well. For low base lengths, the speed dependence corresponds to that of equation 1.3, with the line width w replaced by b, with a lower linear scaling factor. If the data for $b < 1.2$ mm is fitted with the function:

$$\frac{h_{max}}{b} = k \cdot \mathrm{Ca}^{\beta},$$

this results in the values $\beta = 0.32 \pm 0.01$, and $k = 0.21 \pm 0.02$. Especially for the exponent, the correspondence $\beta \approx 1/3$ is remarkable, for this value is derived for the dip-coating of narrow lines, a steady-state entrainment process, while the coating of the triangles is a intrinsically transient process. For the larger base lengths $b \geq l_C$, the speed dependence of the data resembles the behavior described by equation 1.1 more, much like the rivulets with comparable widths.

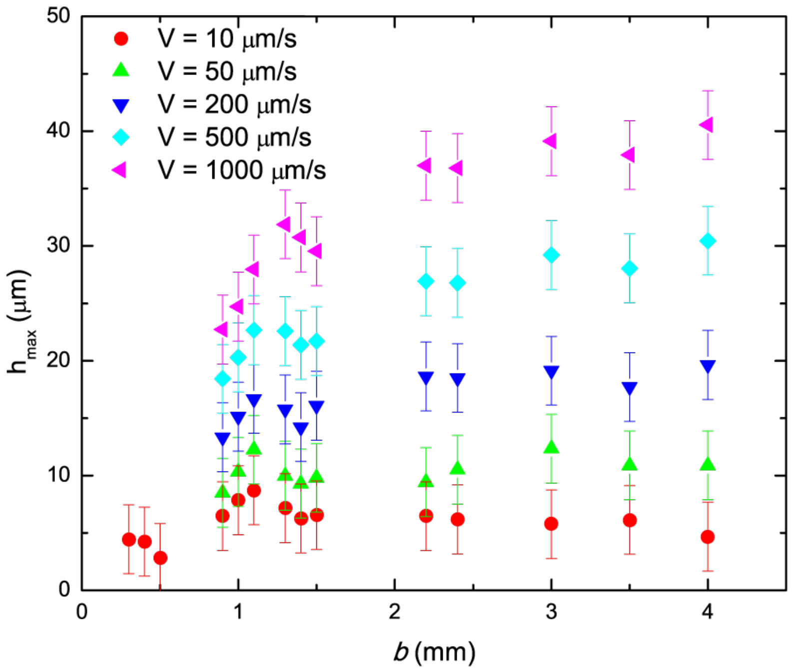

Figure 4.3: Maximum film thickness versus the base length; dip-coated triangles for various coating velocities V.

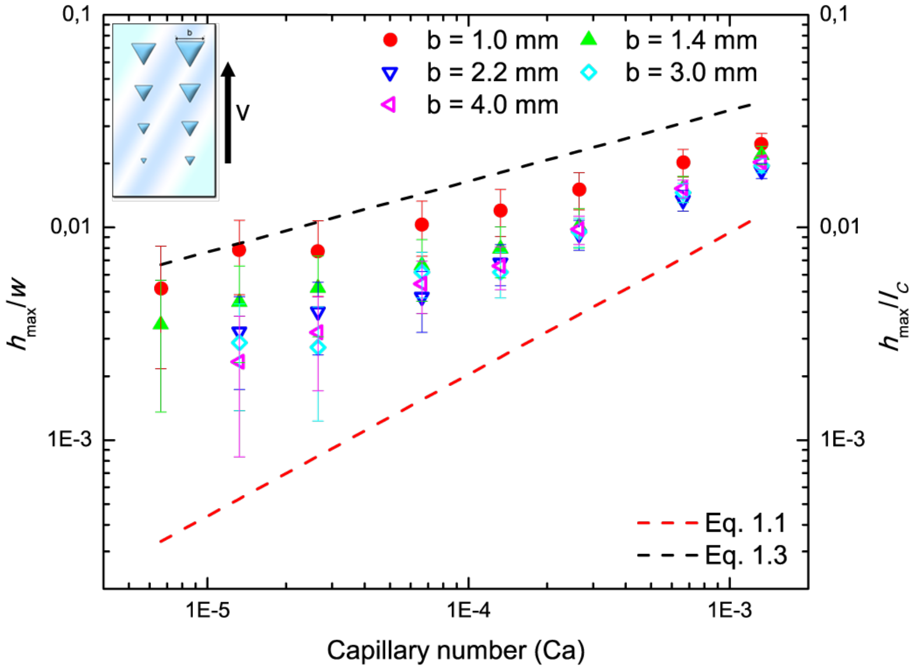

Figure 4.4: Normalized film thickness versus the capillary number; dip-coated triangles of various base length b.

4.4 Dip-coating of squares

The maximum film thickness of the entrained liquid as a function of the coating speed was measured for squares with base lengths varying from 0.50 – 2.50 mm, 0.50 l_C – 1.25 l_C. The coating speeds ranged from 2 – 4000 μm/s. h_{max} was measured by calculating the position of the centroid and measuring the film thickness at that location. The measured thickness was normalized with respect to the dominant length scale: b for base lengths $b < l_C$, plotted on the left ordinate axis with opaque symbols, and l_C for base lengths $b \geq l_C$, plotted on the right ordinate axis with open symbols. The measured film thickness versus the base length is plotted in figure 4.6, and the normalized film thickness versus the capillary number is plotted in figure 4.7. The dashed lines are given by equations 1.1 and 1.3.

As with the triangles, for large base lengths, the entrained film thickness saturates at a speed dependent value. The measured maximum height relates relatively well with equations 1.1 and 1.3 for Ca $\gtrsim 2 \cdot 10^{-3}$, which too is comparable to the coating behavior of the triangles. In the lower regime of b however, h_{max} appears to saturate. This phenomenon is not observed in the triangular patterns, raising the hypothesis that the difference in meniscus break-up effects of both patterns was involved.
To study this behavior further, the maximum height of squares with a fixed base $b = 4.0$ mm and varying inclination angles $0° \leq \phi \leq 45°$ was measured for low values of Ca. The normalized data is depicted in figure 4.8. Due to the rather large error bars, no firm conclusions regarding the meniscus break-up effect can be drawn from this data. Figure 4.9 depicts the cross-section parallel to the coating direction of two squares with inclination angles 0°, a square, and 45°, a diamond. The relative height of the droplets is shown versus the relative width. This data was measured by taking the sample directly out from the dip-coater without letting in equilibrate. Note the symmetrical curve of the diamond, and the asymmetric curve of the square, indicating that the orientation of the square indeed affects coating process.

We attribute this phenomenon to the fact that, at the moment the meniscus of the liquid reservoir breaks up with the meniscus of the entrained droplet, the liquid bridge between the reservoir and the droplet is split in two, and a fragment of this liquid is pulled towards the droplet. This effect is depicted in figure 4.5. The amount of added liquid is independent from the capillary number, but is proportional to the physical dimensions of the droplet meniscus at that location. The result is a negligible contribution for high values of Ca, but a dominant one for low values, resulting in an horizontal asymptote in the limit of Ca → 0.
As stated in section 4.3, the triangles are coated in a 'tip-down' position, leaving the total contact area between the entrained droplet and the meniscus of the reservoir relatively small compared to the triangular pattern. The same argument applies for the rivulets. Conclusive evidence about the influence of the break-up effect requires more research. In particular, the data in figure 4.8 need to be expanded, or alternatively, measurements can be done with triangles in a 'tip-up' position and compared to the data in figure 4.4.

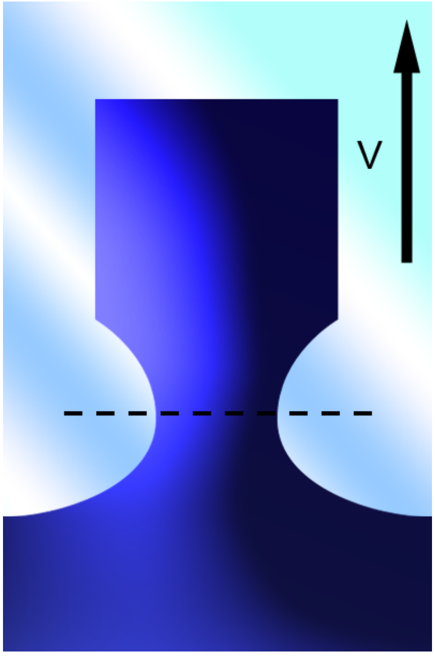

Figure 4.5: At the moment the meniscus breaks, a part of the liquid bridge is pulled towards the square.

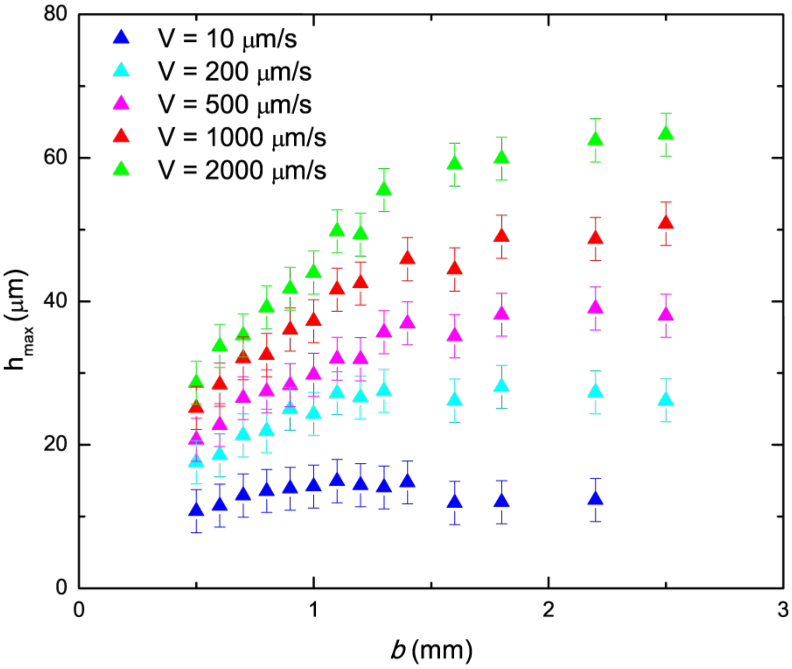

Figure 4.6: Maximum film thickness versus the base length; dip-coated squares for various coating velocities V.

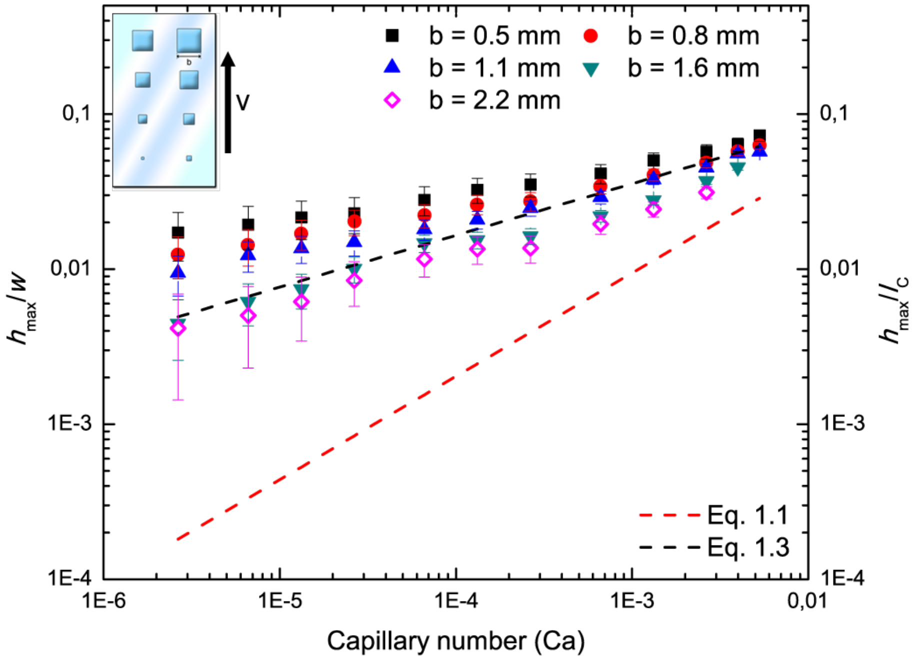

Figure 4.7: Normalized film thickness versus the capillary number; dip-coated squares of various base length b.

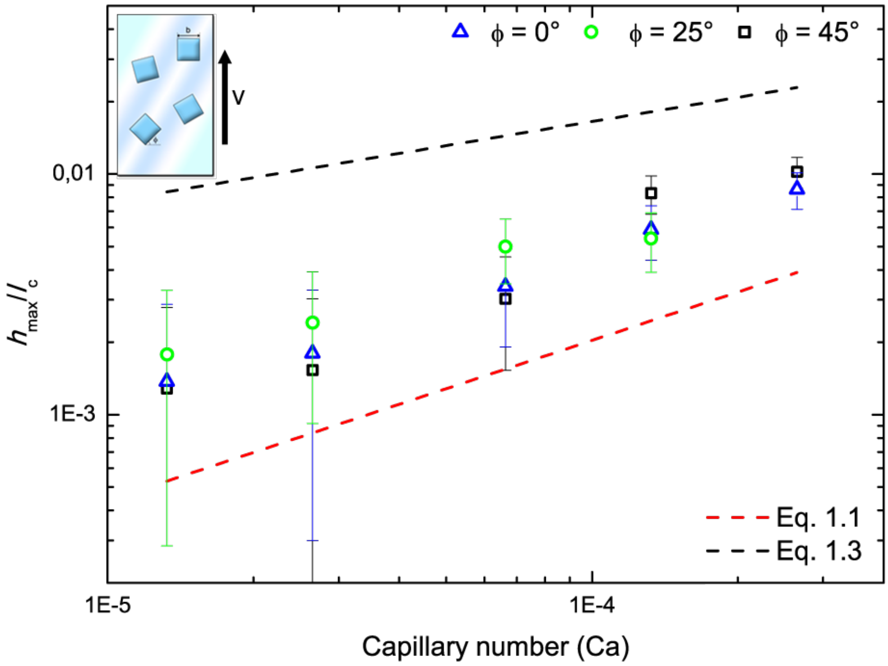

Figure 4.8: Normalized film thickness versus the capillary number; dip-coated squares of various inclination angle ϕ.

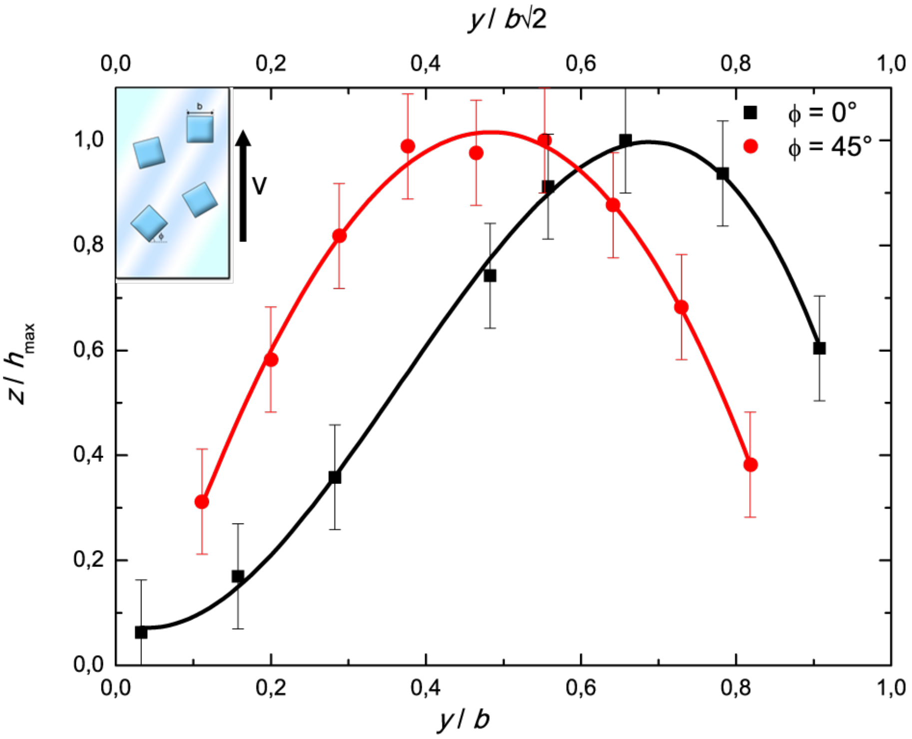

Figure 4.9: Relative height versus the relative width; a dip-coated square (black line, bottom ornate axis) and diamond (red line, top ornate axis)/ The asymmetric curve for the square indicates a meniscus break-up effect.

4.5 Die-coating with varying coating speeds

The maximum film thickness of the entrained liquid as a function of the coating speed was measured for triangles and squares with base lengths varying from 0.50 – 4.00 mm, or 0.25 l_C – 2.0 l_C. The coating speeds ranged from 20 – 500 μm/s for the triangles, and 50 μm/s to 2000 μm/s for the squares, while the die-gap is held constant at $h_0 = 200\mu$m. h_{max} was measured by calculating the position of the centroid and measuring the film thickness at that location. The data is plotted in figure 4.11 and figure 4.12. The dashed lines are given by equations 1.1 and 1.3 and serve as a guide. The triangles are coating in a 'tip-down' position, as seen in the figure. The data was fitted with the function:

$$h_{max} = k \cdot h_0 \cdot \mathrm{Ca}^{\beta}.$$

The values for β are plotted against the base lengths in figure 4.13.

The results for die-coating triangles and squares are very similar to those for dip-coating the same patterns. For the triangles at low base lengths (i.e. $b = 0.5$ mm), the behavior is much like that of equation 1.3. Higher base lengths residing in the region $b \leq 1.6$ mm yield a behavior that is expected from this transition region, where β increases to the value of 2/3, as given by equation 1.4. Increasing the capillary number even higher gives exponents as high as 2. The resemblance to the dip-coating behavior appears to stop here. The reason for this is unknown to the author at this moment, and is a suggested field of further study.

For the squares, the influence of the meniscus break-up effect, as noted in section 4.4, is apparent in the data. Snapshots of the die-coating of a square in which this effect can be observed are shown in figure 4.10. Furthermore, β behaves comparable to the triangles for $b \leq 2.5$ mm. Afterwards the similarity breaks down, with β decreasing for 2 mm $\leq b \leq$ 4 mm.
It is noted that some of the measured film thicknesses h_{max} of large base lengths and coating speeds are larger than the die-gap. This may be caused by the entrained droplets not having minimized their surface energy completely yet at the moment they are cut off from the reservoir. During the energy minimization, the maximum height may grow larger than the die-gap. It is also possible that the high coating speeds in combination with the meniscus break-up effect somehow make the die-coater deposit the liquid differently. Further research is needed to give a conclusive answer.

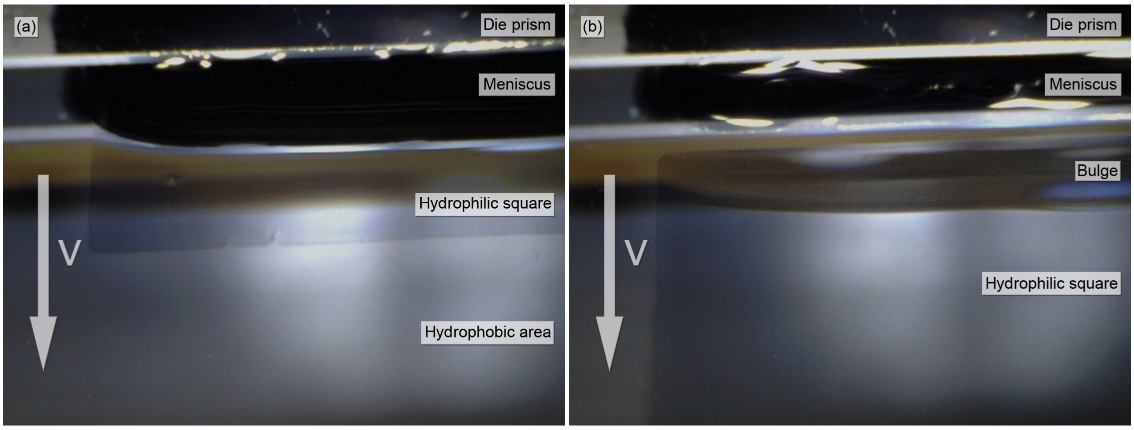

Figure 4.10: Snapshots of the meniscus break-up effect for the die-coating of a square: (a) while coating the square; (b) just after the meniscus breaks.

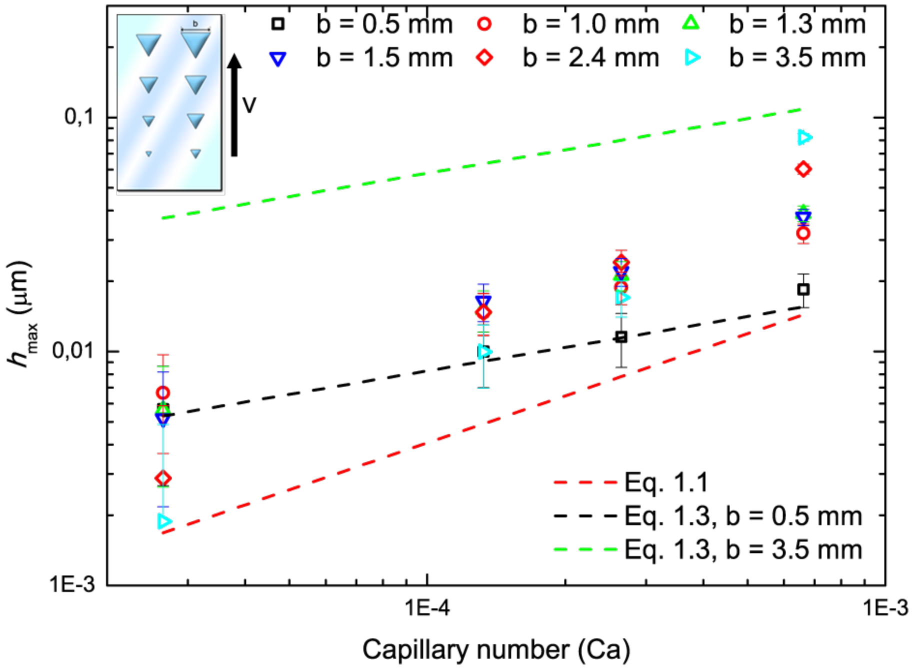

Figure 4.11: Maximum film thickness versus the capillary number; die-coated triangles of various base length b.

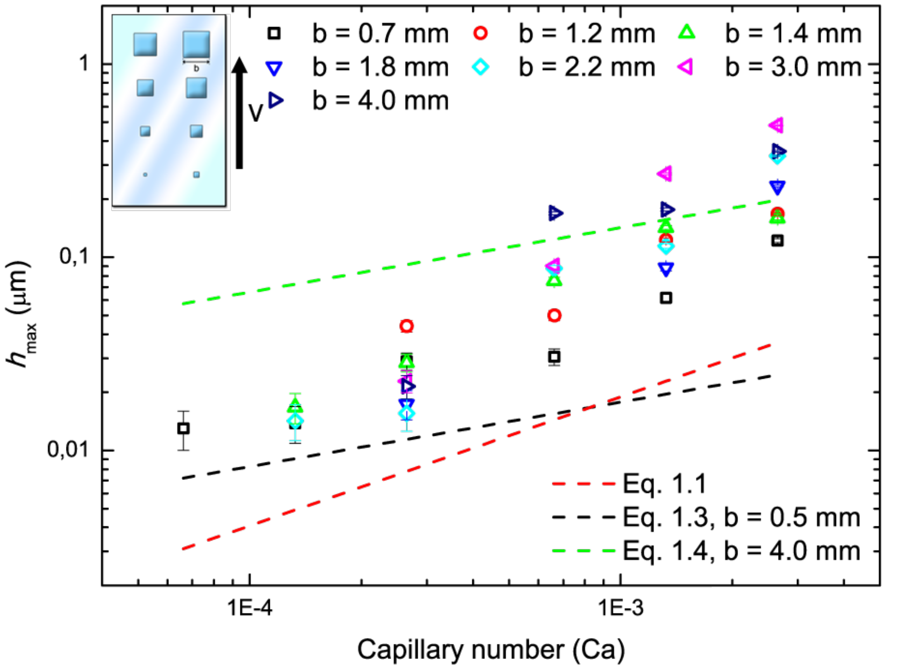

Figure 4.12: Maximum film thickness versus the capillary number; die-coated squares of various base length b.

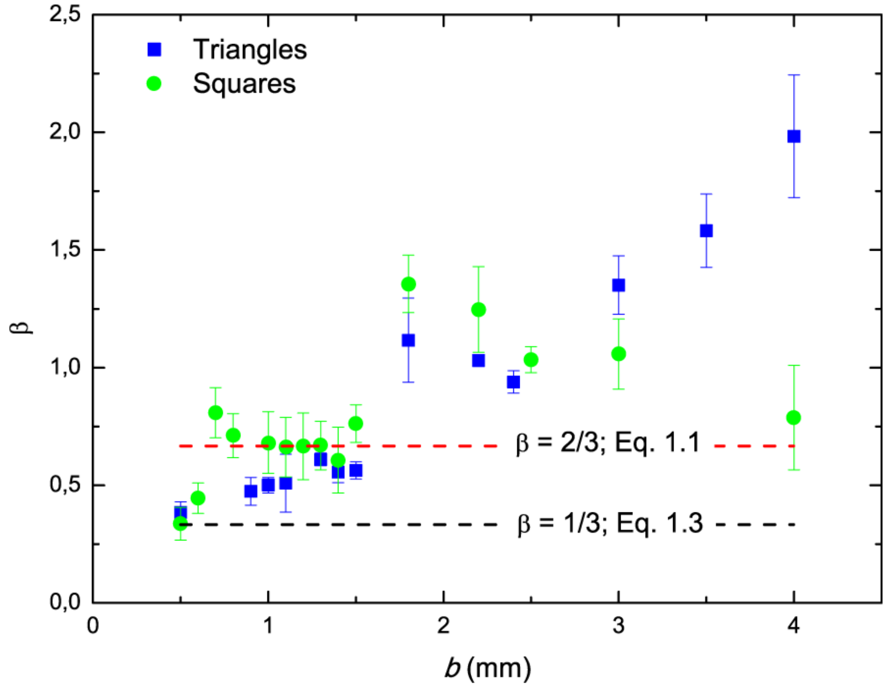

Figure 4.13: The exponent of the speed dependence β versus the base length b for die-coated triangles and squares.

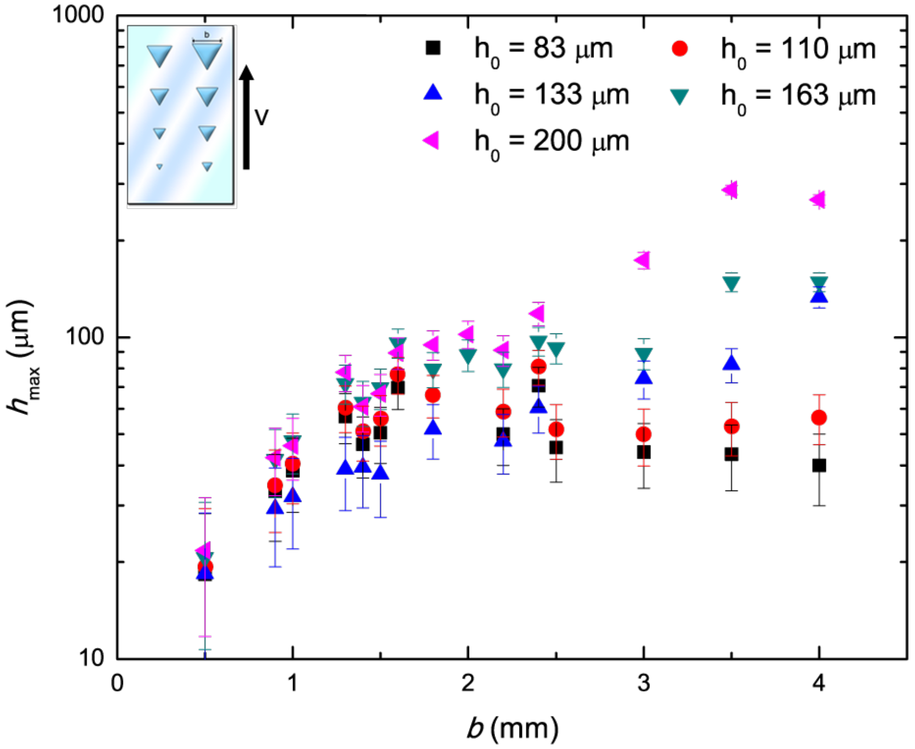

Figure 4.14: Maximum film thickness versus the base length b for die-coated triangles and squares of various die-gaps h_0.

4.6 Die-coating with varying die-gaps

The maximum film thickness of the entrained liquid as a function of the die-gap was measured for triangles base lengths varying from 0.50 – 4.00 mm, or 0.25 l_C – 2.0 l_C. The coating speed was 100 μm/s, while the die-gap is varied between $h_0 = 83 - 200$ μm. h_{max} was measured by calculating the position of the centroid and measuring the film thickness at that location. The data is plotted in figure 4.14. The triangles are coating in a 'tip-down' position, as seen in the figure.

The graph shows that for large base lengths, the entrained film thickness saturates to a value dependent on the die-gap. Larger die-gaps constitute larger saturation values, as is expected from equation 1.4. At small base lengths, the film thickness of the various die-gaps converge to the same linear relation with the base length. As the relevant length scale slowly shifts from the die-gap towards the base length, the coating process shifts to that of the dip-coating of small rivulets in equation 1.3. Further research is required for die-gaps between than 200 – 2000 μm to draw more solid conclusions regarding the influence of the die-gap.

Chapter 5

Summary and conclusions

We have studied the dip and die-coating of chemically patterned surfaces, consisting of a hydrophobic background, with various hydrophilic patterns. The patterns that were used were straight thin rivulets oriented parallel with respect to the coating direction, triangles oriented tip-down, and squares in various orientations. All measurements were done with capillary numbers between $10^{-6} < \mathrm{Ca} < 10^{-3}$.

For dip-coating of all these patterns, we observed a transition in the relation between the maximum entrained film thickness and the capillary number, depending on the size of the patterns. For small patterns relative to the capillary length of the coater fluid, the entrained film thickness was proportional to $\mathrm{Ca}^{1/3}$, as was predicted by theory for the thin lines, and was a contingency for the triangles and squares. For patterns approximately equal to the capillary length, a transition to the theory for large homogeneous substrates was observed, in where the film thickness scales with $\mathrm{Ca}^{2/3}$. We also observed a decrease in the measured height for pairs of rivulets where the meniscus for both patterns overlapped.
Moreover, we observed an increase in film thickness for the squares, especially for lower capillary numbers. This was attributed to the destruction of the liquid bridge between the entrained bubble and the reservoir at the moment of release, from which a part of the liquid is appended to the bubble. It was hypothesized that this effect is relates to the physical dimensions of the bubble, and is independent of the capillary number. For the squares, these physical dimensions were large, and as a result, the break-up effect was large. For the triangles and rivulets, these dimensions were small, and the effect was negligible. Further research needs to be done in order to confirm this.

For die-coating, the influence of both the capillary number and the die-gap on the entrained film thickness of triangles and squares was studied. For small patterns relative to the capillary length of the coater fluid, the entrained film thickness appeared to be proportional to $\mathrm{Ca}^{1/3}$, though few measurements were done in this regime, due to experimental difficulties. For patterns larger than that, but smaller than the capillary length, a transition to the theory for large homogeneous substrates was observed, in where the film thickness scales with $\mathrm{Ca}^{2/3}$. For patterns up to twice the capillary length, the scaling factor increased up to 2. The reason for this is unknown and is suggested as further research.
We also observed the meniscus break-up effect for the die-coating of squares, but not for the triangles, analogously to the dip-coating experiments. Lastly, we observed that larger die-gaps resulted in larger entrained film thicknesses, and that for large patterns this thickness saturated at a value dependent of the die-gap, as was predicted by the theory. Moreover, we observed that the film thickness was less dependent on the value of the die-gap for smaller patterns, because the relevant length scale there shifted from the die-gap to the pattern dimensions.

Bibliography

[1] B.J. Brasjen, A.W. van Cuijk, and A.A. Darhuber. Dip-coating of chemically patterned surfaces. *Chem. Eng. and Proc.*, 50:565–568, 2011.

[2] Dow Chemical Company. Physical properties of ethylene glycols.

[3] A.A. Darhuber, S.M. Troian, J.M. Davis, and S.M. Miller. Selective dipcoating of chemically micro-patterned surfaces. *J. Appl. Phys.*, 88:5119–5126, 2000.

[4] J.M. Davis. Asymptotic analysis of liquid films dip-coated onto chemically micropatterned surfaces. *Phys. Fluids*, 17, 2005.

[5] B. Deryaguin. Thickness of a liquid layer adhering to walls of vessels on their emptying and the theory of photo- and motion picture coating. *Competes Rendus de l' Académie des Sciences de l'URSS*, 39:13–16, 1943.

[6] S. Hartland. volume 119 of *Surfactant science series.* Marcel Dekker, 2004.

[7] L. Landau and B.G. Levich. Dragging of a liquid by amoving plate. *Acta Physicochim. URSS*, 17:42–52, 1942.

[8] A. Pal and W. Singh. Speeds of sound and viscosities in aqueous poly(ethylene glycol) solutions at 303.15 and 308.15 K. *J. Chem. Eng. Data.*, 42:234–237, 1997.

[9] C.W. Park. Effects of insoluble surfactants on dip-coating. *J. Colloid Interface Sci.*, 146:382–394, 1991.

[10] F.L. Pedrotti, L.M. Pedrotti, and L.S. Pedrotti. *Introduction to optics.* Pearson, 2007.

[11] J.J. van Rossum. Viscous lifting and drainage of liquids. *Appl. Sci. Res.*, page 121, 1958.

[12] K.J. Ruschak. Asymptotic analysis of liquid films dip-coated onto chemically micropatterned surfaces. *Chem. Eng. Sci.*, 31:1057–1060, 1976.

[13] J. Schmit. An introduction to non-contact surface metrology, 2013.

[14] N. Tiwari and J.M. Davis. Theoretical analysis of the effect of insoluble surfactant on the dip-coating of chemically micropatterned surfaces. *Phys. Fluids*, 18, 2006.

[15] D. White and J.A. Tallmadge. Theory of drag out of liquids on flat plates. *Chem. Eng. Sci.*, 20:33–37, 1965.

[16] S.D.R. Wilson. The drag-out problem in film coating theory. *J. Eng. Math*, 16:209–221, 1982.

Appendix A

Calculation of centroid position

The calculation of the maximum height for the droplets was calculated using a TI-83 Plus graphical calculator. The pseudocode for the calculations of triangles is given in block A.1. The calculation for squares and rivulets are done in a simular way.

(`x1`,`y1`,`z1`), (`x2`,`y2`,`z2`), and (`x3`,`y3`,`z3`) are the coordinates of the corners of the triangle, and (`x0`,`y0`,`z0`) are the coordinates of the centroid of the triangle on the surface of the glass substrate. The variable `check` is used as a verification and should be equal to the triangle base b. Subsequently, `zm` is the measured height at the calculated centroid. Finally, the height of the droplet `h` is calculated, where the extra factors `4` and `1000` are required for the horizontal to vertical motion conversion of the z-stage, and the conversion to micrometers, respectively.

```
input x1, y1, z1;
input x2, y2, z2;
input x3, y3, z3;

var check = (sqrt((x1-x2)^2 + (y1-y2)^2 + (z1-z2)^2) + sqrt((x2-x3)^2 + (y2-y3)^2 +
     (z2-z3)^2) + sqrt((x3-x1)^2 + (y3-y1)^2 + (z3-z1)^2))/3$;
var x0 = (x1+x2+x3) / 3;
var y0 = (y1+y2+y3) / 3;
var z0 = (z1+z2+z3) / 3;

output check, x0, y0;

Input zm;

var h = (z0 - zm) / 4 * 1000;

output h;
```

Listing A.1: Pseudocode used to calculate the maximum height h_{max} *of a triangle with corners* $(x, y, z)_1$, $(x, y, z)_2$, *and* $(x, y, z)_3$, *and bubble height* z_m.